Lawrence Berkeley National Laboratory

Title
Suppression of Voltage Decay through Manganese Deactivation and Nickel Redox Buffering in High-Energy Layered Lithium-Rich Electrodes

Permalink
https://escholarship.org/uc/item/4jq7n330

Journal
Advanced Energy Materials, 8(21)

ISSN
1614-6832

Authors
Ku, Kyojin
Hong, Jihyun
Kim, Hyungsub
et al.

Publication Date
2018-07-01

DOI
10.1002/aenm.201800606

Peer reviewed

Article type: Full Paper

Suppression of voltage decay through manganese deactivation and nickel redox buffering in high-energy layered lithium-rich electrodes

Kyojin Ku[†], Jihyun Hong[†], Hyungsub Kim, Hyeokjun Park, Won Mo Seong, Sung-Kyun Jung, Gabin Yoon, Kyu-Young Park, Haegyeom Kim, Kisuk Kang*

K. Ku, Dr. J. Hong, Dr. H. Kim, H. Park, W. M. Seong, S.-K. Jung, G. Yoon, Dr. K.-Y. Park, Dr. H. Kim, Prof. K. Kang

Department of Materials Science and Engineering, Research Institute of Advanced Materials, Seoul National University, Seoul 151-742, Republic of Korea. E-mail: matlgen1@snu.ac.kr

Dr. H. Kim

Korea Atomic Energy Research Institute (KAERI), 111 Daedeok-daero 989 Beon-Gil, Yuseong-gu, Daejeon 34057, Republic of Korea

K. Ku, H. Park, S.-K. Jung, G. Yoon, Prof. K. Kang

Center for Nanoparticle Research, Institute of Basic Science (IBS), Seoul National University, Seoul 151-742, Republic of Korea.

†These authors contributed equally to this work.

Abstract

 Cobalt-free layered lithium-rich nickel manganese oxides, $Li[Li_xNi_yMn_{1-x-y}]O_2$, are promising positive electrode materials for lithium rechargeable batteries because of their high energy density and low materials cost. Utilization of the oxygen anionic redox in this series of materials enables realization of a high capacity beyond that achieved *via* the conventional transition metal cationic redox when charging above 4.5 V *vs.* Li/Li^+. However, substantial voltage decay is inevitable upon electrochemical cycling, which makes this class of materials less practical. It has been proposed that this undesirable voltage decay is linked to irreversible structural rearrangement involving irreversible oxygen loss and cation migration. Herein, we demonstrate that the voltage decay of the electrode is correlated to Mn^{4+}/Mn^{3+} redox activation and subsequent cation disordering, which can be remarkably suppressed *via* simple compositional tuning to induce the formation of Ni^{3+} in the pristine material. By implementing our new strategy, the Mn^{4+}/Mn^{3+} reduction is subdued by an alternative redox reaction involving the use of this pristine Ni^{3+} as a redox buffer, which has been designed to be widened from Ni^{3+}/Ni^{4+} to Ni^{2+}/Ni^{4+}, without compensation for the capacity in principle. Negligible change in the voltage profile of the modified lithium-rich nickel manganese oxide electrode is observed upon extended cycling, and manganese migration into the lithium layer is significantly suppressed. Based on these findings, we propose a general strategy to suppress the

voltage decay of Mn-containing lithium-rich oxides to achieve long-lasting

high energy density from this class of materials.

1. Introduction

One of the grand challenges facing green energy technologies such as electric vehicles and large-scale power backups is the need to achieve a breakthrough enhancement of the energy density in current lithium-ion batteries.[1] As a key step forward, great efforts have been made to develop electrode materials with higher reversible capacities. Among the various cathode materials investigated to date, layered lithium-rich nickel manganese oxides (Li[Li$_x$Ni$_y$Mn$_{(1-x-y)}$]O$_2$, 0 < x < 0.33, 0 < y < 0.5; hereafter called LLNMOs) are of particular interest because of their extraordinarily high reversible capacities (> 250 mAh g^{-1}) and relatively high operating voltage (~3.6 V vs. Li/Li$^+$).[2] Nevertheless, one of the critical issues encountered with the use of LLNMOs is the inevitable voltage decay, or the progressive decrease of the operating voltage with electrochemical cycling, which leads to a gradual loss of the energy density. This voltage decay was proposed to originate from a structural transformation involving a spinel-like disordered phase via cation migration during cycling and the activation of the Mn^{4+}/Mn^{3+} redox reaction in the lower-potential region, which reduces the overall voltage.[3, 4] This claim was supported by Bo et al.[5], who identified lithium ions in tetrahedral sites and the migration of transition metal ions in a high-resolution electron microscopy study, suggesting the formation of a spinel-like domain. Yabuuchi et al.[6] also observed a bulk structural rearrangement, which included cation migration from the transition metal layer to the lithium layer, in lithium-rich layered $3d$ metal oxides in an X-

ray diffraction (XRD) study. Recently, Gent et al.[7] used XRD and various spectroscopies to show that the cation migration in lithium-rich manganese-based metal oxides is coupled with the anion redox.

 Sathiya et al.[8, 9] further elucidated the issue of cation migration in lithium-rich layered oxides using the simpler $Li_2Ru_{1-x}M_xO_3$ (M=Mn, Ti, Sn) system; these authors demonstrated that the voltage decay can be suppressed by substitution with Sn^{4+} ions, which inhibit the cation migration because of their large size. As the authors hypothesized that the ion size was a critical factor in the cation migration, they speculated that it would be difficult to mitigate the voltage fade for LLNMOs or 3d metal oxides because of the intrinsically small ionic size of 3d metal cations and their relatively high stability in tetrahedral sites.[10, 11] In this regard, more focus has recently shifted to the discovery of new lithium-rich materials based on 4d and 5d metals beyond 3d-metal-based oxides and LLNMOs, with the identification of a few important lithium-rich electrode materials.[7, 11-17] Although these fundamental scientific studies on this series of new materials provide essential steps toward the development of high-energy-density cathodes capable of exploiting both the cation and anion redox reactions[18], these materials are still far from being considered for practical application because of the use of rare and heavy metals. In addition, the high raw material cost and relatively low energy density significantly dilute the potential merits of this class of lithium-rich layered materials.

In this respect, we highlight the importance of a careful revisit of the suppression of the voltage decay of practically viable lithium-rich materials composed of nickel and manganese. We note that the oxygen anion redox has never been reported to be a completely reversible process; there is always a partial permanent loss of oxygen from the material during the charge process *via* the oxygen gas evolution.[19-21] The partial loss of the oxygen redox capability requires an additional redox couple to compensate for the capacity, which typically induces the reduction of Mn^{4+} to Mn^{3+} during the following discharge of the LLNMO electrode. For example, in the representative LLNMO, $Li_{1.2}Ni^{2+}_{0.2}Mn^{4+}_{0.6}O_2$ (or $Li_2Mn^{4+}O_3–LiNi^{2+}_{0.5}Mn^{4+}_{0.5}O_2$), the initial oxidation state of manganese is +4, which is maintained even during charging, accompanying the oxidation of oxygen over 4.5 V *vs*. Li/Li^+; however, during the discharge, Mn^{4+} needs to be partially reduced to Mn^{3+} in the re-lithiation process because of the partial loss of the anionic redox activity, as schematically illustrated in **Figure 1**a and c. Unfortunately, Mn^{3+} is known to be vulnerable to migration, which results in the layered-to-spinel phase transformation.[22, 23] The relatively small crystal field stabilization energy difference in octahedral and tetrahedral coordinations and the disproportionation into Mn^{2+} and Mn^{4+} generally facilitate the migration of Mn^{3+} into the lithium layer.

Herein, we demonstrate that the introduction of Ni^{3+} as a redox buffer through a simple substitution of Mn with Ni in $Li_{1.2}Ni^{2+}_{0.2}Mn^{4+}_{0.6}O_2$ (or $Li_2Mn^{4+}O_3–LiNi^{2+}_{0.5}Mn^{4+}_{0.5}O_2$) effectively suppresses the Mn reduction and

7

voltage decay of this LLNMO without the use of 4d transition metals or doping with third heavy elements. To inhibit the reduction of Mn^{4+} to Mn^{3+} during the re-lithiation after the partial loss of the oxygen redox couple, we activate the Ni^{3+}/Ni^{2+} reduction process alternatively in the modified LLNMO electrode. It is demonstrated that the substitution of nickel increases the nickel oxidation state in the pristine compounds from 2+ ($Li_{1.2}Ni^{2+}_{0.2}Mn^{4+}_{0.6}O_2$) to 3+ ($Li_{1.2}Ni^{3+}_{0.4}Mn^{4+}_{0.4}O_2$ or $Li_2Mn^{4+}O_3–LiNi^{3+}O_2$) and that the electrochemical reduction of the increased quantity of Ni^{3+} replaces the Mn^{4+} reduction during the discharge process because of its higher redox potential in layered materials. Moreover, it is revealed that after the activation of the nickel redox buffer, it undergoes a full Ni^{2+}/Ni^{4+} redox reaction to compensate for the partial loss of the oxygen redox in the subsequent cycles. Although various LLNMO compositions have been previously explored in extensive studies[24, 25], we believe that this strategy of activating the widened nickel redox reaction and mitigating the unfavorable manganese redox will provide clearer guidance in the design and compositional tailoring of LLNMO electrodes with practically high energy densities.

2. Results and Discussion

The proposed redox mechanisms of LLNMOs with two representatively different compositions and the potential role of Ni^{3+} as a redox buffer are schematically illustrated in Figure 1. Notably, even with the substitution

and increased oxidation state of nickel, the initial charging capacity contributed by the nickel cationic redox reaction remains the same, with the redox mechanism relying on 0.4 of the Ni^{3+}/Ni^{4+} single redox (0.4 e$^-$) in $Li_{1.2}Ni^{3+}_{0.4}Mn^{4+}_{0.4}O_2$ (Figure 1b) or 0.2 of the Ni^{2+}/Ni^{4+} double redox (0.4 e$^-$) in $Li_{1.2}Ni^{2+}_{0.2}Mn^{4+}_{0.6}O_2$ (Figure 1a). After the partial loss associated with the anionic redox reaction, Mn^{4+} must be reduced to Mn^{3+} during the full re-lithiation in $Li_{1.2}Ni^{2+}_{0.2}Mn^{4+}_{0.6}O_2$ (Figure 1c). However, Ni^{3+} reduces to Ni^{2+} in $Li_{1.2}Ni^{3+}_{0.4}Mn^{4+}_{0.4}O_2$ because of the empty Ni^{2+}/Ni^{3+} state in the density of states (DOS) below the Mn^{3+}/Mn^{4+} state during the re-lithiation process, and therefore, the Ni^{2+}/Ni^{3+} state potentially plays the role of a redox buffer, as illustrated in Figure 1d. The subsequent cycles of the $Li_{1.2}Ni^{3+}_{0.4}Mn^{4+}_{0.4}O_2$ electrodes would then be available, utilizing both the Ni^{2+}/Ni^{3+} and Ni^{3+}/Ni^{4+} redox reactions instead of the single-electron Ni^{3+}/Ni^{4+} reaction in the pristine electrode. The additional activation of the nickel redox reaction fully compensates for the capacity loss from the subdued manganese redox reaction, which is also beneficial because of the higher redox potential of Ni^{2+}/Ni^{3+} than Mn^{3+}/Mn^{4+}.

We performed proof-of-concept experiments using a series of LLNMO compounds (zLi_2MnO_3–$(1-z)LiMO_2$) with a fixed amount of Li_2MnO_3 (z = 0.5) and systematic adjustment of the nickel to manganese ratio in $LiMO_2$ (M = $Ni_{0.5}Mn_{0.5}$, $Ni_{0.75}Mn_{0.25}$, and Ni). The chemical compositions of the target compounds were thus $Li_{1.2}Ni_yMn_{0.8-y}O_2$ (y = 0.2, 0.3, and 0.4; hereafter called LL226, LL235, and LL244, respectively). Relative ratio between lithium, nickel and manganese of the synthesized compounds

were determined to be 1.20: 0.22: 0.67 (LL226), 1.20: 0.32: 0.56 (LL235) and 1.20: 0.43: 0.44 (LL244), respectively, using inductively coupled plasma-atomic emission spectroscopy (ICP-AES), in consistent with the target compositions. For the clarity, the amount of residual lithium impurities was quantified by titration technique, where it was found they were all comparable with the value obtained from the stoichiometric $LiNi_{0.6}Co_{0.2}Mn_{0.2}O_2$ which has been known to have little issue with residual lithium.[26] Both X-ray diffraction (XRD) and neutron diffraction (ND) patterns of the three compounds confirmed that they were O3-type layered structures; the diffraction patterns were indexed to the $R\bar{3}m$ symmetry with the superstructure patterns of the *C2/m* symmetry without impurities (**Figure 2**a and 2b).[2] The superstructure patterns in the 2θ range of 20–25° for the XRD analysis originated from the honeycomb-like transition-metal–lithium ordering (*e.g.* $LiMn_6$) in the transition metal layers.[27, 28] The weaker superstructure pattern in LL244 compared with that in LL226 suggests the more random atomic configuration in the transition metal layers of LL244 with less manganese content, which has a strong tendency to form $LiMn_6$ domains.[29, 30] The ND patterns of the LLNMO compounds varied more appreciably with the compositional changes than the XRD patterns because of the larger difference in the neutron scattering lengths of nickel (10.3 fm) and manganese (−3.73 fm), [31] as shown in Figure 2b. The intensities of the (003) peak at 22.4° and (104) peak at 53.6° gradually increased with increasing nickel content. This observation is consistent with the ND simulation results presented in

10

Figure S1 and is attributed to the stronger scattering of neutrons by nickel than manganese. The lattice parameters and atomic occupancies of the LLNMO compounds were determined using Rietveld refinement of the XRD and ND patterns, and the results are summarized in Tables S1–S5 and Figure S2 and S3. Systematic changes in the lattice parameters following Vegard's law were observed[32], which are indicative of the gradual changes in the Ni/Mn ratio within the lithium-rich layered framework. The X-ray absorption near-edge structure (XANES) of the Ni K-edge revealed that with increasing nickel content, the nickel ions of the pristine materials displayed higher oxidation states (Figure S4 and **Figure 3**d). This finding agrees with the targeted oxidation states of +2, +2.67, and +3 for LL226, LL235, and LL244, respectively. In contrast, as observed in the Mn K-edge spectra, the oxidation states of manganese remained unchanged at +4 for all of the compounds regardless of the Ni/Mn ratio (Figure S4 and Figure 3a).

We comparatively measured the electrochemical activities of the series of LLNMO electrodes to monitor the intrinsic behaviors of the voltage fade as a function of cycling. To accelerate the potential structural evolution and voltage decay, we employed relatively harsh cycling conditions: a low current density of 20 mA g^{-1} at 60 °C in the voltage range of 2.0–4.8 V (Figure 2c–i and S5). During the initial charging process, all the LL226, LL235, and LL244 electrodes exhibited the characteristic plateau of lithium-rich layered oxide electrodes at 4.4–4.5 V, indicating that the oxidation of oxygen commonly occurred, as shown in Figure S5.[19, 33, 34] The

initial charging capacities were 357, 352, and 343 mAh g^{-1}, respectively, corresponding to almost all the lithium being extracted from the materials (> ~1.1 Li$^+$ per formula unit). However, unlike the similar first charge profiles, the discharge profiles already began to show suppressed voltages, particularly for LL226. The distinct voltage decay behaviors for the samples are apparent in Figure 2c, which compares the charge/discharge profiles of the electrodes after five cycles. The voltage decay progressed most significantly in the LL226 electrode, with the appearance of a pseudo plateau at 3.2 V in the charge profile, consistent with previous reports[24, 35]. This finding suggests that the Mn^{4+}/Mn^{3+} redox reaction was active, which was most likely accompanied by a significant structural transformation followed by partial oxygen loss. In contrast, the voltage profiles of the electrodes with higher Ni^{3+} contents were stably maintained. LL244 exhibited the highest discharge voltage with an average value of 3.57 V, comparable to the initial discharge voltage, and LL235 exhibited an average discharge voltage of 3.54 V without the presence of the 3.2-V activity typically observed in manganese-containing lithium-rich layered oxide electrodes. For more quantitative analysis of the voltage fade with cycling, the electrochemical profiles of each electrode for 40 cycles are presented in Figure 2d, f, and h along with the differential capacity *vs.* voltage plots in Figure 2e, g, and i. Figure 2d, f, and h clearly show that the voltage decay was substantially reduced for LL244 and LL235 in sharp contrast to clear voltage fade of LL226 with cycling. Even though the voltage profiles of LL244 appear to be similar to those of

12

LL235 in terms of the voltage decay, the differential capacity plots (Figure 2g and 2i) clearly reveal that LL244 was more effective for suppression, as indicated by the dotted line, which shows the least shift to lower voltage. It is also possible to find same trend at the 80 cycle test at 1C rate, where LL244 shows much less voltage decay than LL226 (Figure 2C inset and S6). This finding confirms that the voltage decay was significantly subdued with increasing Ni^{3+} content; the role of Ni^{+3} will be discussed in more detail in the following sections. We note that these trends were also observed in previous reports on the electrochemical properties of various lithium-rich nickel manganese oxides, although their origin remained elusive.[24, 25, 36]

To clarify the redox mechanisms and understand the distinctive behaviors of the LLNMO electrodes, *ex situ* X-ray absorption spectroscopy (XAS) was performed for each sample during cycling. Figure 3a–f present the XANES spectra of the Mn K-edge and Ni K-edge for the three electrodes in pristine, charged, and discharged states. The Mn K-edge spectra in Figure 3a indicate that the oxidation states of Mn were identical as +4 for the pristine LL226, LL235, and LL244 electrodes and remained unchanged during the charging process, as illustrated in Figure 3b. These findings support the claim that the manganese redox reaction does not occur during the first charge process. However, the discharge process apparently induced different manganese redox activity for the samples, as shown in Figure 3c. The reduction of Mn^{4+} to Mn^{3+} was clearly observed for LL226, which is consistent with previous findings.[6, 35, 37] However, the Mn^{4+}

reduction was substantially suppressed in LL235 and LL244, and the most effective suppression was observed for LL244, which nearly maintained the initial Mn^{4+} state. These findings were further confirmed by X-ray photoelectron spectroscopy (XPS) experiments, which supported the claim that more extensive manganese reduction occurred in LL226 than in LL244 after electrochemical cycling (Figure S7).

The spectra at the Ni K-edge in Figure 3e–f further highlight the different redox behaviors of the three samples. Figure 3d shows that the nickel oxidation states were initially +2, +2.67, and +3 for the pristine LL226, LL235, and LL244 electrodes, respectively, in accordance with expectations based on their nominal compositions. Upon charging to 4.8 V, all of the Ni K-edge spectra shifted to the same edge energy corresponding to the Ni^{4+} state (Figure 3e), confirming the double redox reaction of Ni^{2+}/Ni^{4+} in the LL226 electrode and the single redox of Ni^{3+}/Ni^{4+} in the LL244 electrode. During discharge, the spectra shifted back to lower energy, indicative of the reduction of Ni^{4+} ions; however, all the samples were identically reduced to the Ni^{2+} state at the end of discharge (Figure 3f), in clear contrast with the initially different nickel oxidation states. This finding strongly suggests that the redox reaction of nickel ions in LL244 (or LL235) was extended from Ni^{3+}/Ni^{4+} (or $Ni^{2.67+}/Ni^{4+}$) to Ni^{2+}/Ni^{4+} after the first cycle (more clear comparisons are presented in Figure S8). The widened electrochemical redox activity of nickel coincides with the suppressed manganese redox reaction in LL244 (or LL235), supporting the claim that a subdued Mn^{3+}/Mn^{4+} reaction in LLNMO electrodes can be

achieved by tailoring the nickel redox activity, which serves as a redox buffer after the partial loss of the oxygen anionic redox. The universal observation of the activation of redox couples originally inactive in LLNMOs, which necessitates loss of the reversible oxygen redox couple, indicates the minimal change in the stability of the oxygen anion redox with the substitution of nickel while further work is required for better understanding. The activation of the additional Ni^{2+}/Ni^{3+} redox reaction in LL244 and LL235 after the first cycle also accounts for the high electrochemical activities at 3.7 V of the samples without loss of the capacity in the absence of manganese redox activity. It is noteworthy that the redox reaction of Ni^{3+}/Ni^{2+} instead of Mn^{4+}/Mn^{3+} could occur during the discharge because of its higher redox potential, as illustrated in Figure 1.

To elucidate the observed difference in the voltage decay and the effect of the nickel redox buffer, structural analyses were performed for each LLNMO sample after cycling using high-resolution transmission electron microscopy (HR-TEM) and XRD. **Figure 4**a and b compare the local atomic structure of the LL226 electrode before and after cycling in the zone axis along the $[-441]_R$//$[10-1]_M$ (R and M represent the rhombohedral $R\bar{3}m$ and monoclinic *C2/m* structures, respectively) direction, which is also parallel to the [001] direction of cubic *Fd-3m.* Although the pristine LL226 electrode exhibited the structure of typical lithium-rich layered oxides with domains of $R\bar{3}m$ and *C2/m* structures, as shown in Figure 4a, additional diffraction spots (highlighted with red circles) are clearly observed after

15

cycling, as shown in Figure 4b. These additional diffraction spots can be better visualized in the intensity histogram of the red boxed region shown in the inset; they cannot be assigned to any planes of the layered phase but can be indexed as the {220} planes of the cubic spinel phase.[38] The $(220)_C$ plane is distinguished from the parallel planes of the layered phase by the presence of transition metals in the lithium layers (Figure S9), thereby indicating the formation of disordered domains, which is indicative of significant interlayer migration of transition metal ions in LL226 after cycling. Similar observations were made in other regions of particles, as shown in Figure S10; these findings are consistent with those presented in previous reports on LLNMOs, implying the correlation between the activated manganese redox activity and the transition migration.[4, 5, 38, 39] In contrast, the cycled LL244 electrode did not exhibit a notable signature of the local phase transformation involving transition metal migration, preserving the pristine layered framework, as observed in Figure 4c and d. The additional $(220)c$ spots that were easily detected in the cycled LL226 electrode were not detectable along the same zone axis in the HR-TEM analysis of the cycled LL244 electrodes. This apparently different behavior in the local structure change was also confirmed in XRD patterns, as shown in Figure S11, which indicated that the cycled LL244 electrode exhibited a much lower degree of cation disordering than the cycled LL226 and LL235 electrodes, suggesting the structural integrity of LL244 as a layered structure after cycling.

We further examined the changes in the atomic arrangements of the

samples after cycling using Raman spectroscopy, which has been demonstrated to be particularly sensitive to changes in metal–oxygen bonds in layered and disordered layered (or spinel) structures.[4, 21, 40, 41] Figure 4e compares the Raman spectra of the LL226, LL235, and LL244 electrodes after electrochemical cycling. Initially, all three samples exhibited similar patterns characteristic of layered structures with a trace of Li_2MnO_3-like domains (Figure S12). However, after cycling, notable differences were observed in the spectra. Most importantly, the symmetrical M–O stretching peak of the pristine structure split into two peaks near 627 and 572 cm^{-1}, which were attributed to symmetrical stretching (A_{1g}) in the spinel-like $Li_{1+x}M_2O_4$ structure and the A_{1g} mode of the pristine layered structure that appears at relatively lower frequency, respectively[42] (see Figure S12 in the supporting information for further details). This finding suggests the coexistence of two different bonding environments (*i.e.,* phases) after electrochemical cycling, which is consistent with previous studies on LL226.[4, 5] Moreover, the ratio between the A_{1g} peaks of the spinel-like and layered phases sensitively depended on the composition of the LLNMO compounds. The LL244 compound contained the lowest fraction of the spinel-like phase, which is consistent with the previously presented TEM and XRD results. The calculated portions of the spinel A_{1g} peak area to the total peak area were 57%, 48%, and 22% for LL226, LL235, and LL244, respectively, which confirms that the structure remained intact as a layered structure for the LL244 electrode even after electrochemical cycling in contrast to the cycled

LL226 electrode.

Based on the observations above, we propose the following mechanism for the electrochemical redox reactions occurring in the LLNMO electrodes with and without the Ni^{3+} redox buffer. During the first charge, the initial delithiation (> ~ 4.4 V) occurs *via* the oxidation of Ni^{2+} (LL226), $Ni^{2.67+}$ (LL235), or Ni^{3+} (LL244) to Ni^{4+}, accounting for the 0.4 Li^+ ion extraction from each electrode. The remaining 0.8 Li^+ ions are further delithiated with the concurrent oxidation of the oxygen, corresponding to the observed plateau at ~4.4–4.5 V (*vs.* Li/Li^+) for all the electrodes. At the end of charge, the valence states of both nickel and manganese are +4 regardless of the Ni/Mn ratios in the LLNMO electrodes. Upon discharge, the re-lithiation involves the cationic reduction of nickel along with possible oxygen anionic reduction. However, when the loss of the oxygen anionic redox activity occurs due to irreversible oxygen gas evolution or other possible mechanisms that remain elusive,[6, 19-21, 43-45] the subsequent re-lithiation occurs at different cationic redox centers in each LLNMO electrode. For the LL226 electrode containing the least amount of nickel, Mn^{4+} serves as an additional redox center to compensate for the loss of the oxygen anionic redox. However, for the LL244 electrode, the extra redox contribution can originate from the Ni^{3+}/Ni^{2+} redox because of the presence of the Ni^{3+} redox buffer, which is sufficiently rich to compensate for the loss of the partial oxygen anionic redox. Because the redox potential of Ni^{2+}/Ni^{3+} lies above that of Mn^{3+}/Mn^{4+}, it is possible to suppress the contribution of the manganese redox activity in the LLNMO with the

Ni^{+3} redox buffer. For the LL235 electrode, some portion of the Mn^{4+} reduction to Mn^{3+} may occur simultaneously for the full re-lithiation. As the Mn^{3+} ions are subsequently prone to inducing the layered to disordered spinel-like phase transformation,[22, 23] the additional Mn^{3+} in the cycled electrode facilitates the formation of the disordered spinel-like phase and induces a stronger voltage fade such as in the LL226 electrode. In contrast, the cycled LL244 electrode, which does not require the manganese reduction, can better maintain the layered phase, thereby avoiding the voltage depression. Presently, it is unclear whether the manganese reduction leads to the transition migration or whether the transition migration gives rise to the partial manganese redox activity; this issue should be addressed in a future study.[7] In this regard, a recent study on sodium lithium manganese layered oxides, $Na_{0.6}[Li_{0.2}Mn_{0.8}]O_2$, with P3-type structure where the oxygen is proposed to be the only redox couple, is noted in that no voltage decay and reversible voltage plateaus are observed.[46] Nevertheless, the results of our study indicate that the suppression of the manganese reduction by the introduction of the nickel redox buffer could significantly suppress the structural disordering and voltage decay, offering clearer guidance in the design and compositional tailoring of Li-rich layered oxides.

3. Conclusion

In summary, we proposed a new strategy to suppress the voltage decay

in LLNMO electrodes by introducing a Ni^{3+} redox buffer that can subdue the redox activity of manganese and its migration in the layered structure. Investigations of a series of LLNMO electrodes confirmed that introduction of the Ni^{3+} redox buffer led to significant reduction of the voltage decay during cycling, successfully preserving the pristine layered structure. The suppression of the voltage decay was correlated to a decrease in the Mn^{3+} content resulting from the Mn^{4+} reduction during the discharge reaction, which could be systematically tailored by the presence of the Ni^{3+} redox buffer, enabling extended nickel redox activity from Ni^{3+}/Ni^{4+} to Ni^{2+}/Ni^{4+} after the partial loss of the oxygen anionic redox. The findings of this study suggest that to suppress the voltage decay of layered lithium-rich transition metal oxides, it is critical to deal with the cation migration that induces the formation of the disordered spinel-like domain. In addition, tailoring of the oxidation states of nickel and manganese not only in the pristine states but also during electrochemical cycling can offer an effective way to prevent the voltage decay in LLNMOs without the use of 4d or 5d elements.

4. Experimental Section

Sample Preparation: $0.5Li_2MnO_3–0.5LiNi_xMn_{1-x}O_2$ (x = 0.5, 0.75, 1), i.e., $Li_{1.2}Ni_yMn_{0.8-y}O_2$ (y = 0.2, 0.3, 0.4), were prepared using a solid-state reaction from lithium carbonate and nickel manganese carbonate ($Ni_yMn_{1-y}CO_3$, y = 0.25, 0.375, 0.5). The mixed nickel manganese

carbonate was prepared *via* a co-precipitation method. A 0.2 M mixed nickel sulfate and manganese sulfate aqueous solution (Ni:Mn = 2:6, 3:5, 4:4) was added dropwise to an equal volume of a 1 M $NaHCO_3$ aqueous solution under constant stirring (250 rpm) at 50 °C. The pH was maintained at pH 9 by adding an appropriate amount of NH_4OH. The $(NiMn)CO_3$ precipitate was filtered, rinsed with deionized water several times, and dried overnight at 120 °C. The obtained powder was mixed with lithium carbonate; 3 wt% excess lithium carbonate compared with the stoichiometric amount was added to compensate for the possible lithium evaporation at high temperature. The mixture was heated at 900 °C for 6 h in air and then quenched by soaking the powder in liquid nitrogen.

Characterization of Compound: The chemical formulas of the synthesized compounds were determined using ICP-AES (Thermo Jarrel Ash, Polyscan 60E, USA). The crystal structures of the layered Li-excess nickel manganese oxides were characterized using a D/MAX-2500 X-ray diffractometer (Rigaku, Japan) equipped with Cu-Kα radiation (λ = 1.54178 Å) in the 2θ range of 10–75°. ND data were collected over the 2θ range of 15–155° with a step size of 0.05°, and λ = 1.8348 Å was supplied by a Ge (331) single-crystal monochromator on a high-resolution powder diffractometer (HRPD) at the HANARO facility at the Korea Atomic Energy Research Institute. The amount of residual lithium was measured by titration method (888 Titrando, Metrohm)

Electrochemical Measurements: The electrodes were fabricated by casting a slurry paste consisting of 80 wt% active materials, 10 wt% carbon black (Super P), and 10 wt % polyvinylidene fluoride onto aluminum foil, which was used as the current collector. Coin-type cells (CR2016, Hohsen, Japan) were assembled using the electrodes, a Li metal counter electrode, a separating membrane (Celgard 2400), and a 1 M solution of $LiPF_6$ in a mixture of ethyl carbonate and dimethyl carbonate (EC/DMC, 1:1 v/v) as the electrolyte in an Ar-filled glove box. The galvanostatic charging/discharging process was performed at 60 °C at 20 mA g^{-1} in the voltage range of 2.0−4.8 V using a potentio-galvanostat (WonA Tech, WBCS 3000, Korea).

Ex situ Characterization: For the ex situ experiments, the electrodes were retrieved by disassembling the tested cells and rinsing with DMC. The procedures were performed in an Ar-filled glove box. XPS spectra were obtained using an X-ray photoelectron spectrometer (Sigma Probe, Thermo VG Scientific, England) with an Al-Kα (1487 eV) X-ray source. Ni and Mn K-edge XAS spectra were collected at the BL10C beamline at the Pohang Light Source (PLS) at the Pohang Accelerator Laboratory, Korea. A Si(1 1 1) double crystal was employed to monochromatize the X-ray photon energy. The monochromator was detuned to 35–45% of its original intensity to eliminate the high-order harmonics. Mn and Ni K-edge spectra were collected in transmission mode. Energy calibration was performed using the first inflection point of the spectra of Mn and Ni metal foils as a reference (i.e., Mn K-edge = 6539 eV and Ni K-edge = 8333 eV). Reference

spectra were simultaneously collected for each *in situ* spectrum using Mn or Ni metal foils. The electrode samples were prepared by disassembling the coin cells after the electrochemical cycling and sealing them in a water-resistant polymer film in the Ar-filled glove box. Analysis of the XAS spectra was performed using the IFEFFIT software package.[47]

Supporting Information

Supporting information is available from the Wile Online Library or from the author.

Acknowledgments

References

[1]   K. Kang, Y. S. Meng, J. Bréger, C. P. Grey, G. Ceder, *Science* **2006**, *311*, 977.

[2]   Z. Lu, D. D. MacNeil, J. R. Dahn, *Electrochem. Solid-State Lett.* **2001**, *4*, A191.

[3]   J. Hong, H. Gwon, S.-K. Jung, K. Ku, K. Kang, *J. Electrochem. Soc.* **2015**, *162*, A2447.

[4]   J. Hong, D.-H. Seo, S.-W. Kim, H. Gwon, S.-T. Oh, K. Kang, *J. Mater. Chem.* **2010**, *20*, 10179.

[5]   B. Xu, C. R. Fell, M. Chi, Y. S. Meng, *Energy Environ. Sci.* **2011**, *4*, 2223.

[6]   N. Yabuuchi, K. Yoshii, S.-T. Myung, I. Nakai, S. Komaba, *J. Am. Chem. Soc.* **2011**, *133*, 4404.

[7]   W. E. Gent, K. Lim, Y. Liang, Q. Li, T. Barnes, S.-J. Ahn, K. H. Stone, M. McIntire, J. Hong, J. H. Song, Y. Li, A. Mehta, S. Ermon, T. Tyliszczak, D. Kilcoyne, D. Vine, J.-H. Park, S.-K. Doo, M. F. Toney, W. Yang, D. Prendergast, W. C. Chueh, *Nat. Commun.* **2017**, *8*, 2091.

[8]   M. Sathiya, K. Ramesha, G. Rousse, D. Foix, D. Gonbeau, A. S. Prakash, M. L. Doublet, K. Hemalatha, J. M. Tarascon, *Chem. Mater.* **2013**, *25*, 1121.

[9]   M. Sathiya, A. M. Abakumov, D. Foix, G. Rousse, K. Ramesha, M. Saubanère, M. L. Doublet, H. Vezin, C. P. Laisa, A. S. Prakash, D. Gonbeau, G. VanTendeloo, J. M. Tarascon, *Nat. Mater.* **2015**, *14*, 230.

[10]   A. Grimaud, A. Demortière, M. Saubanère, W. Dachraoui, M.

Duchamp, M.-L. Doublet, J.-M. Tarascon, *Nat. Energy* **2016**, *2*, 16189.

[11]   A. J. Perez, Q. Jacquet, D. Batuk, A. Iadecola, M. Saubanère, G. Rousse, D. Larcher, H. Vezin, M.-L. Doublet, J.-M. Tarascon, *Nat. Energy* **2017**, *2*, 954.

[12]   N. Yabuuchi, M. Takeuchi, M. Nakayama, H. Shiiba, M. Ogawa, K. Nakayama, T. Ohta, D. Endo, T. Ozaki, T. Inamasu, K. Sato, S. Komaba, *Proc. Natl. Acad. Sci.* **2015**, *112*, 7650.

[13]   J. Lee, D.-H. Seo, M. Balasubramanian, N. Twu, X. Li, G. Ceder, *Energy Environ. Sci.* **2015**, *8*, 3255.

[14]   P. E. Pearce, A. J. Perez, G. Rousse, M. Saubanère, D. Batuk, D. Foix, E. McCalla, A. M. Abakumov, G. Van Tendeloo, M.-L. Doublet, J.-M. Tarascon, *Nat. Mater.* **2017**, 16, 580.

[15]   S.-K. Jung, K. Kang, *Nat. Energy* **2017**, *2*, 912.

[16]   C. Zhan, Z. Yao, J. Lu, L. Ma, V. A. Maroni, L. Li, E. Lee, E. E. Alp, T. Wu, J. Wen, Y. Ren, C. Johnson, M. M. Thackeray, M. K. Y. Chan, C. Wolverton, K. Amine, *Nat. Energy* **2017**, *2*, 963.

[17]   S. Kim, M. Aykol, V. I. Hegde, Z. Lu, S. Kirklin, J. R. Croy, M. M. Thackeray, C. Wolverton, *Energy Environ. Sci.* **2017**, *10*, 2201.

[18]   E. McCalla, A. M. Abakumov, M. Saubanère, D. Foix, E. J. Berg, G. Rousse, M.-L. Doublet, D. Gonbeau, P. Novák, G. Van Tendeloo, R. Dominko, J.-M. Tarascon, *Science* **2015**, *350*, 1516.

[19]   J. Hong, H.-D. Lim, M. Lee, S.-W. Kim, H. Kim, S.-T. Oh, G.-C. Chung, K. Kang, *Chem. Mater.* **2012**, *24*, 2692.

[20]   K. Luo, M. R. Roberts, N. Guerrini, N. Tapia-Ruiz, R. Hao, F. Massel, D.

M. Pickup, S. Ramos, Y.-S. Liu, J. Guo, A. V. Chadwick, L. C. Duda, P. G. Bruce, *J. Am. Chem. Soc.* **2016**, *138*, 11211.

[21]   S. Hy, F. Felix, J. Rick, W. N. Su, B. J. Hwang, *J. Am. Chem. Soc.* **2014**, *136*, 999.

[22]   J. Reed, G. Ceder, A. Van Der Ven *Electrochem. Solid-State Lett.* **2001**, *4*, A78.

[23]   S. Choi, A. Manthiram, *J. Electrochem. Soc.* **2002**, *149*, A1157.

[24]   J. C. Knight, A. Manthiram, *J. Mater. Chem. A* **2015**, *3*, 22199.

[25]   S. Chong, Y. Liu, W. Yan, Y. Chen, *RSC Adv.* **2016**, *6*, 53662.

[26]   H.-J. Noh, S. Youn, C. S. Yoon, Y.-K. Sun, *J. Power Sources* **2013**, *233*, 121.

[27]   A. Van der Ven, G. Ceder, *Electrochem. Commun.* **2004**, *6*, 1045.

[28]   Y. S. Meng, G. Ceder, C. P. Grey, W. S. Yoon, M. Jiang, J. Bréger, Y. Shao-Horn, *Chem. Mater.* **2005**, *17*, 2386.

[29]   H. Kobayashi, M. Tabuchi, M. Shikano, H. Kageyama, R. Kanno, *J. Mater. Chem.* **2003**, *13*, 957.

[30]   J. Bréger, M. Jiang, N. Dupré, Y. S. Meng, Y. Shao-Horn, G. Ceder, C. P. Grey, *J. Solid State Chem.* **2005**, *178*, 2575.

[31]   V. F. Sears, *Neutron News* **1992**, *3*, 26.

[32]   L. Vegard, *Z. Phys.* **1921**, *5*, 17.

[33]   A. R. Armstrong, M. Holzapfel, P. Novák, C. S. Johnson, S.-H. Kang, M. M. Thackeray, P. G. Bruce, *J. Am. Chem. Soc.* **2006**, *128*, 8694.

[34]   K. Luo, M. R. Roberts, R. Hao, N. Guerrini, D. M. Pickup, Y.-S. Liu, K. Edström, J. Guo, A. V. Chadwick, L. C. Duda, P. G. Bruce, *Nat Chem* **2016**,

8, 684.

[35]   G. Assat, D. Foix, C. Delacourt, A. Iadecola, R. Dedryvère, J.-M. Tarascon, *Nat. Commun.* **2017**, *8*, 2219.

[36]   J.-L. Shi, J.-N. Zhang, M. He, X.-D. Zhang, Y.-X. Yin, H. Li, Y.-G. Guo, L. Gu, L.-J. Wan, *ACS Appl. Mater. Interfaces* **2016**, *8*, 20138.

[37]   A. Ito, Y. Sato, T. Sanada, M. Hatano, H. Horie, Y. Ohsawa, *J. Power Sources* **2011**, *196*, 6828.

[38]   M. Gu, I. Belharouak, J. Zheng, H. Wu, J. Xiao, A. Genc, K. Amine, S. Thevuthasan, D. R. Baer, J.-G. Zhang, N. D. Browning, J. Liu, C. Wang, *ACS Nano* **2012**, *7*, 760.

[39]   P. Oh, M. Ko, S. Myeong, Y. Kim, J. Cho, *Adv. Energy Mater.* **2014**, *4*, 1400631.

[40]   S.-J. Hwang, H.-S. Park, J.-H. Choy, G. Campet, J. Portier, C.-W. Kwon, J. Etourneau, *Electrochem. Solid-State Lett.* **2001**, *4*, A213.

[41]   S. Loridant, L. Abello, E. Siebert, G. Lucazeau, *Solid State Ionics* **1995**, *78*, 249.

[42]   S.-J. Hwang, H.-S. Park, J.-H. Choy, G. Campet, *Chem. Mater.* **2000**, *12*, 1818.

[43]   N. Tran, L. Croguennec, M. Ménétrier, F. Weill, P. Biensan, C. Jordy, C. Delmas, *Chem. Mater.* **2008**, *20*, 4815.

[44]   F. La Mantia, F. Rosciano, N. Tran, P. Novák, *J. Electrochem. Soc.* **2009**, *156*, A823.

[45]   Y. Xie, M. Saubanere, M. L. Doublet, *Energy Environ. Sci.* **2017**, *10*, 266.

[46]   X. Rong, J. Liu, E. Hu, Y. Liu, Y. Wang, J. Wu, X. Yu, K. Page, Y.-S. Hu, W. Yang, H. Li, X.-Q. Yang, L. Chen, X. Huang, *Joule* **2018**, *2*, 125.

[47]   B. Ravel, M. Newville, *J. Synchrotron Radiat.* **2005**, *12*, 537.

Figures
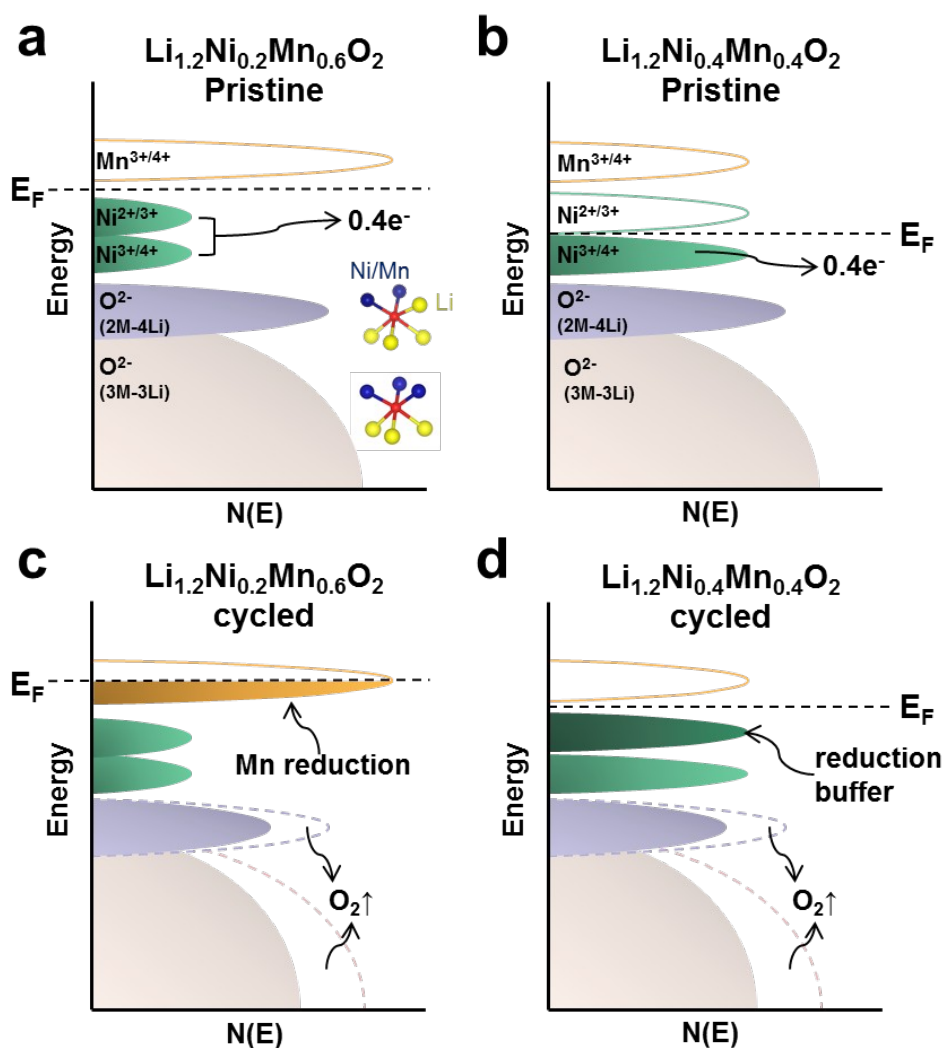
Figure 1. Schematic illustration of electronic structures in LLNMOs. Electronic density of states (DOS) of a) pristine $Li_{1.2}Ni_{0.2}Mn_{0.6}O_2$ (LL226), b) pristine $Li_{1.2}Ni_{0.4}Mn_{0.4}O_2$ (LL244), c) cycled LL226, and d) cycled LL244. The $Ni^{2+/3+}$ states in LL244 act as a reduction buffer, whereas manganese reduction occurs in the cycled LL226.
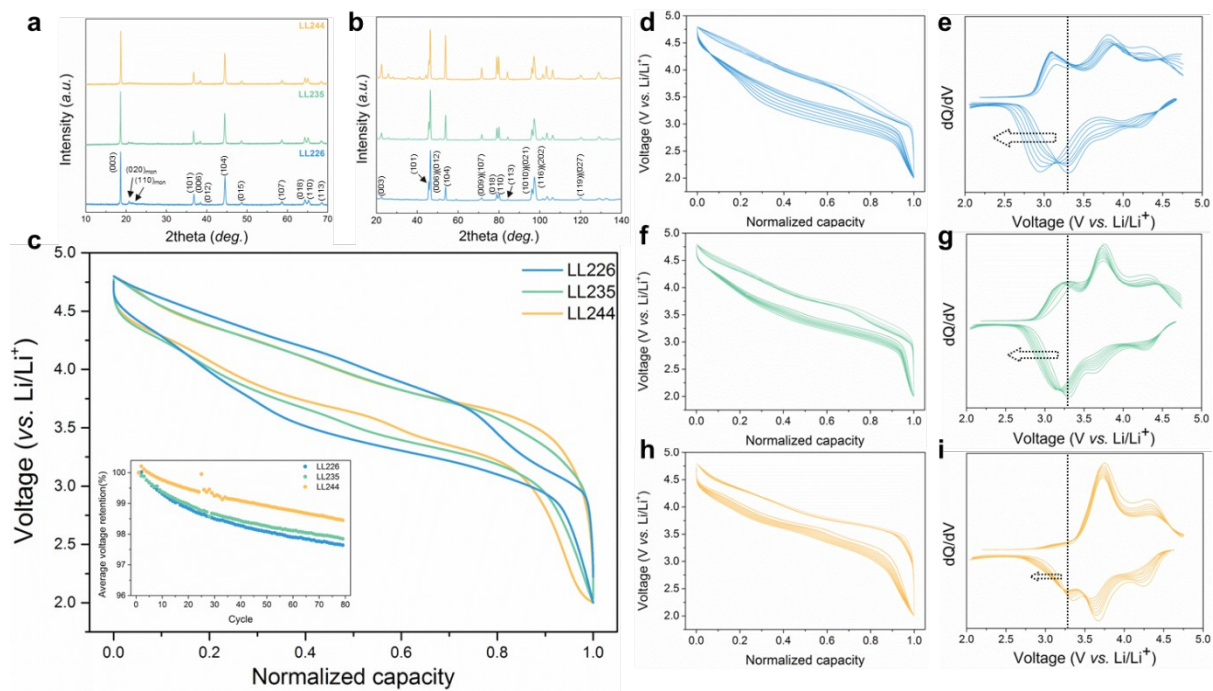
Figure 2. Structures and electrochemical curves of LLNMOs. a) XRD and b) ND patterns of pristine LL226 (blue), LL235 (green), and LL244 (orange). c) Fifth normalized charge/discharge profile of LLNMOs. Inset shows average voltage retention (%) of LLNMOs over cycles at 1C rate. The normalized charge/discharge profile from the 5th to 40th cycles and their dQ/dV plots of d), e) LL226, f), g) LL235 and h), i) LL244. The results are plotted every 5 cycles. The dotted lines in e), g) and i) represent the initial discharge redox potentials of the LLNMOs.
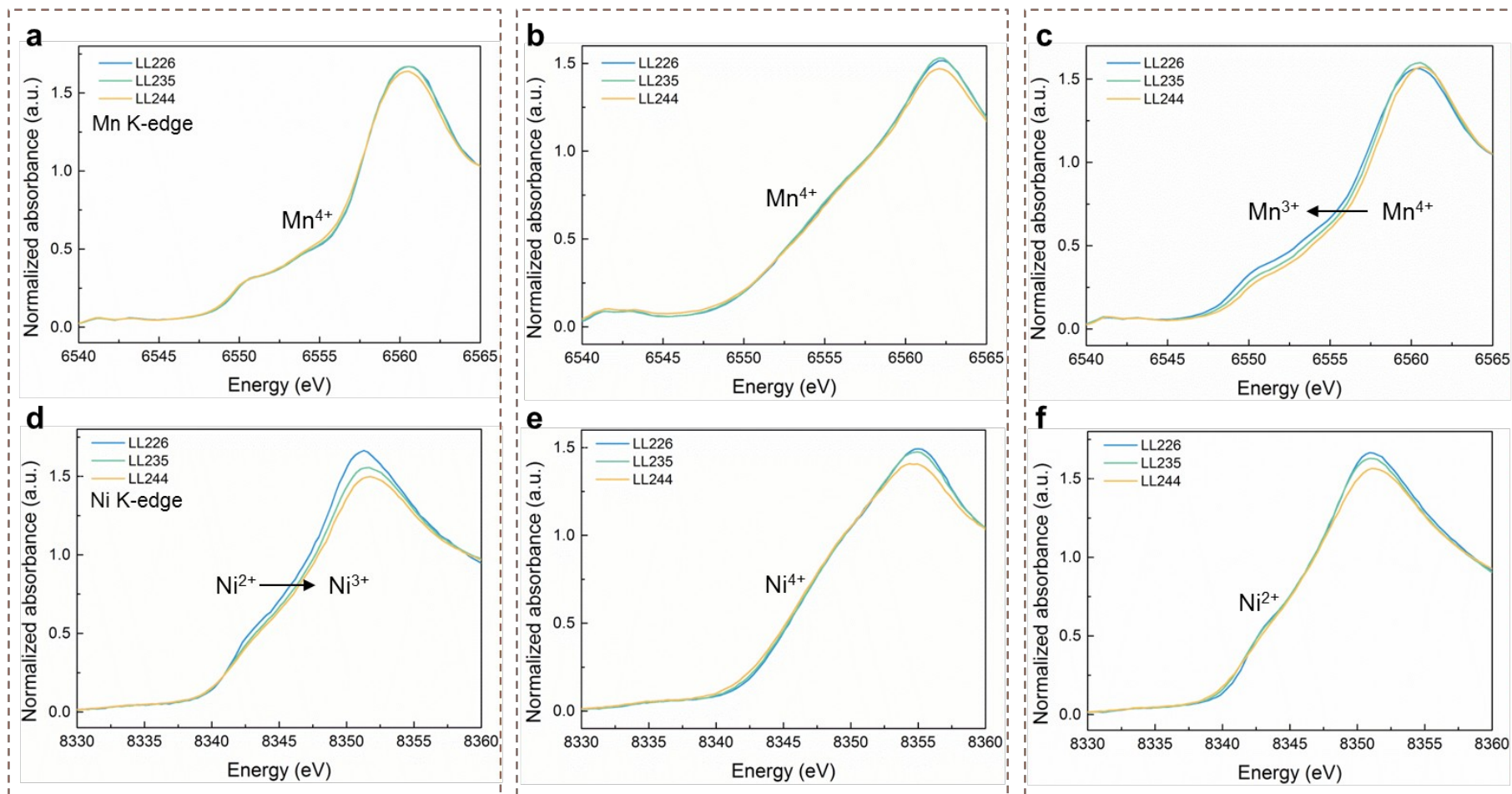
Pristine   **After full charge**   **After full discharge (one cycle)**

Figure 3. Oxidation state changes of nickel and manganese during the first cycle. Mn K-edge XANES spectra of LL226 (blue), LL235 (green), and LL244 (orange) in a) pristine state, b) charged state (4.8 V), and c) discharged state (2.0 V). Ni K-edge XANES spectra of LL226, LL235, and LL244 in d) pristine state e) charged state, and f) discharged state.
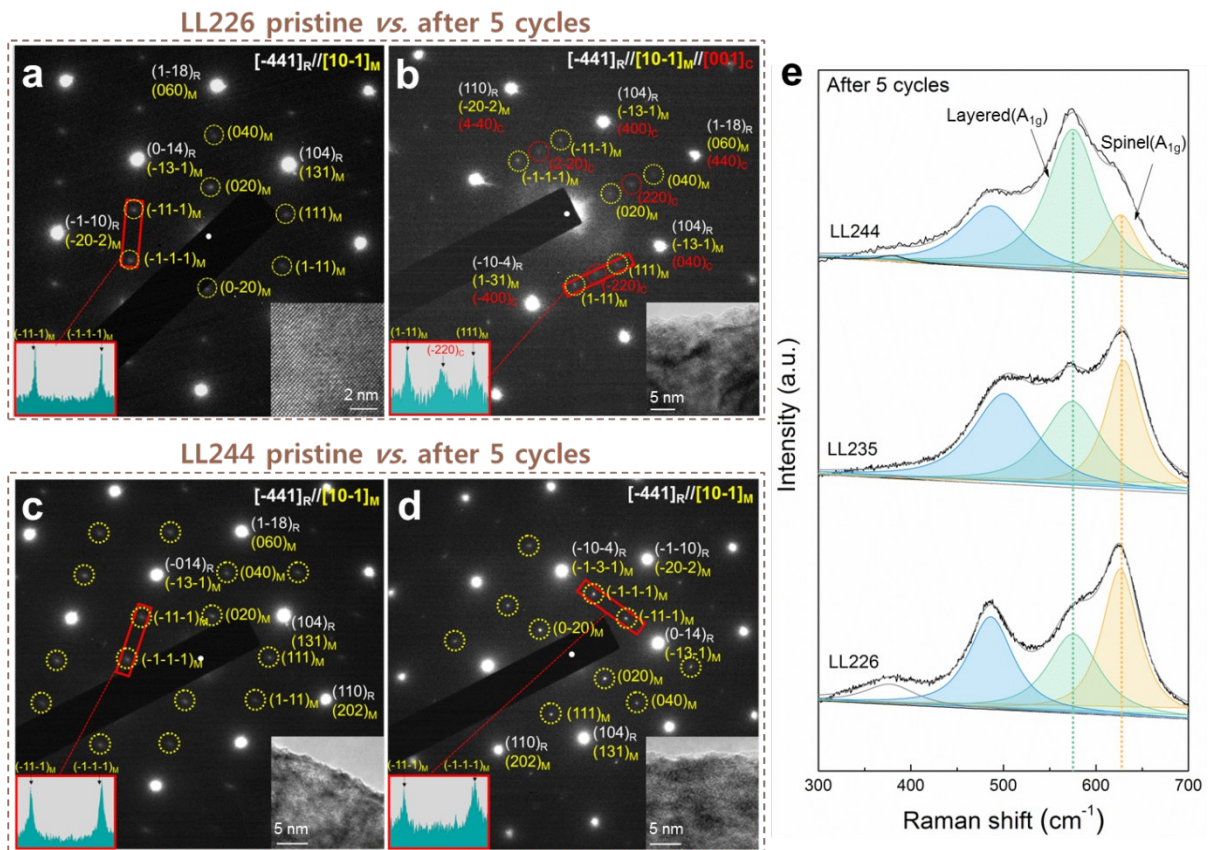
Figure 4. Structural variations in LLNMO after electrochemical cycling. SAED pattern of LL226 a) before and b) after five cycles and that of LL244 c) before and d) after five cycles along the $[-441]_R$ direction, which is parallel to the $[10-1]_M$ direction of monoclinic *C2/m* and $[001]_C$ direction of cubic *Fd-3m* (spinel phase). HR-TEM images and the intensity histograms of the red boxed regions are presented in the insets of the SAED patterns. e) Raman spectra of LLNMOs after five cycles. The orange and green peaks are attributed the A_{1g} mode of the spinel and layered phases, respectively, whereas the blue peaks are attributed both to the E_g mode of the layered phase and F_{2g} mode of the spinel phase.

Key words: layered lithium-rich nickel manganese oxides, voltage decay, redox buffer, Mn deactivation, phase transformation

Kyojin Ku[†], Jihyun Hong[†], Hyungsub Kim, *Hyeokjun Park, Won Mo Seong,*Sung-Kyun Jung, Gabin Yoon, Kyu-Young Park, Haegyeom Kim, Kisuk Kang*

Suppression of voltage decay through manganese deactivation and nickel redox buffering in high-energy layered lithium-rich electrodes
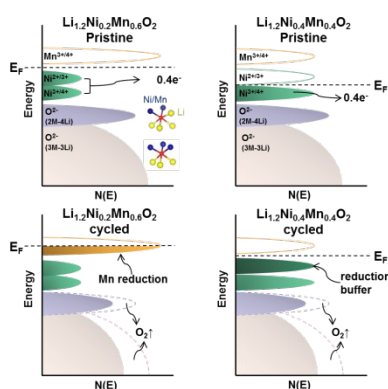
Novel strategy to suppress the voltage decay in layered lithium-rich nickel manganese oxides is demonstrated using Ni redox buffer. A substitution of Mn with Ni in lithium-rich nickel manganese oxides results in the deactivation of Mn reduction, which is compensated by Ni redox reaction. Mn deactivation reduces the undesirable phase transformation, eventually leading to the suppression of the voltage decay.

Supporting Information

Suppression of voltage decay through manganese deactivation and nickel redox buffering in high-energy layered lithium-rich electrodes

Kyojin Ku[†], Jihyun Hong[†], Hyungsub Kim, Hyeokjun Park, Won Mo Seong, Sung-Kyun Jung, Gabin Yoon, Kyu-Young Park, Haegyeom Kim, Kisuk Kang*

Table S1. The detailed data for the structural refinement of LLNMO using XRD patterns

Source	X-ray		
Formula	$Li_{1.2}Ni_{0.2}Mn_{0.6}O_2$	$Li_{1.2}Ni_{0.3}Mn_{0.5}O_2$	$Li_{1.2}Ni_{0.4}Mn_{0.4}O_2$
Crystal system	Rhombohedral	Rhombohedral	Rhombohedral
Space group	$R\bar{3}m$	$R\bar{3}m$	$R\bar{3}m$
Lattice parameters			
a (Å)	2.8586 (2)	2.8616 (2)	2.8662 (2)
c (Å)	14.2611 (24)	14.2519 (17)	14.2477 (15)
Unitcell volume (Å³)	100.922 (22)	101.067 (18)	101.365 (16)
Formula weight	85.03	85.41	85.78
Temperature (K)	300	300	300
Wave length (Å)	1.54059	1.54059	1.54059
2θ range	10 - 80°	10 - 80°	10 - 80°
Number of data points	7000	7000	7000
Step size	0.01°	0.01°	0.01°
R_p (%)	2.55	2.38	2.60
R_I (%)	8.65	6.50	4.90
R_F (%)	7.61	6.55	4.35
χ^2	1.77	1.36	1.93

Table S2. The detailed data for the structural refinement of LLNMO using ND patterns

Source	Neutron		
Formula	$Li_{1.2}Ni_{0.2}Mn_{0.6}O_2$	$Li_{1.2}Ni_{0.3}Mn_{0.5}O_2$	$Li_{1.2}Ni_{0.4}Mn_{0.4}O_2$
Crystal system	Rhombohedral	Rhombohedral	Rhombohedral
Space group	$R\bar{3}m$	$R\bar{3}m$	$R\bar{3}m$
Lattice parameters			
a (Å)	2.8575 (2)	2.8600 (1)	2.8656 (1)
c (Å)	14.2499 (8)	14.2430 (5)	14.2427 (4)
Unitcell volume (Å³)	100.767 (10)	100.892 (5)	101.285 (5)
Formula weight	85.03	85.41	85.78
Temperature (K)	300	300	300
Wave length (Å)	1.834333	1.834333	1.834333
2θ range	0 - 160°	0 - 160°	0 - 160°
Number of data points	3200	3200	3200
Step size	0.05	0.05	0.05
R_p (%)	4.08	3.55	3.23
R_I (%)	4.66	3.28	2.96
R_F (%)	3.84	2.57	2.25
χ^2	7.24	6.71	5.24

Table S3. The atomic positions and occupancies in LL226 using ND patterns

Atom	x	y	z	B$_{iso}$	Occupancy
Li1	0	0	0.5	1.35 (9)	0.96 (1)
Ni1	0	0	0.5	1.35 (9)	0.03 (1)
Li2	0	0	0	0.40 (1)	0.21 (1)
Ni2	0	0	0	0.40 (1)	0.16 (1)
Mn2	0	0	0	0.40 (1)	0.61
O1	0	0	0.2585	1.48 (3)	1.0
			(1)		

Table S4. The atomic positions and occupancies in LL235 using ND patterns

Atom	x	y	z	B$_{iso}$	Occupancy
Li1	0	0	0.5	1.08 (9)	0.97 (1)
Ni1	0	0	0.5	1.08 (9)	0.03 (1)
Li2	0	0	0	0.70 (3)	0.22 (1)
Ni2	0	0	0	0.70 (3)	0.27 (1)
Mn2	0	0	0	0.70 (3)	0.50
O1	0	0	0.2586	0.92 (2)	1.0
			(1)		

Table S5. The atomic positions and occupancies in LL244 using ND patterns

Atom	x	y	Z	B_{iso}	Occupancy
Li1	0	0	0.5	1.3 (1)	0.96 (1)
Ni1	0	0	0.5	1.3 (1)	0.02 (1)
Li2	0	0	0	0.36 (7)	0.21 (1)
Ni2	0	0	0	0.36 (7)	0.38 (1)
Mn2	0	0	0	0.36 (7)	0.4
O1	0	0	0.2583 (1)	0.49 (2)	1.0
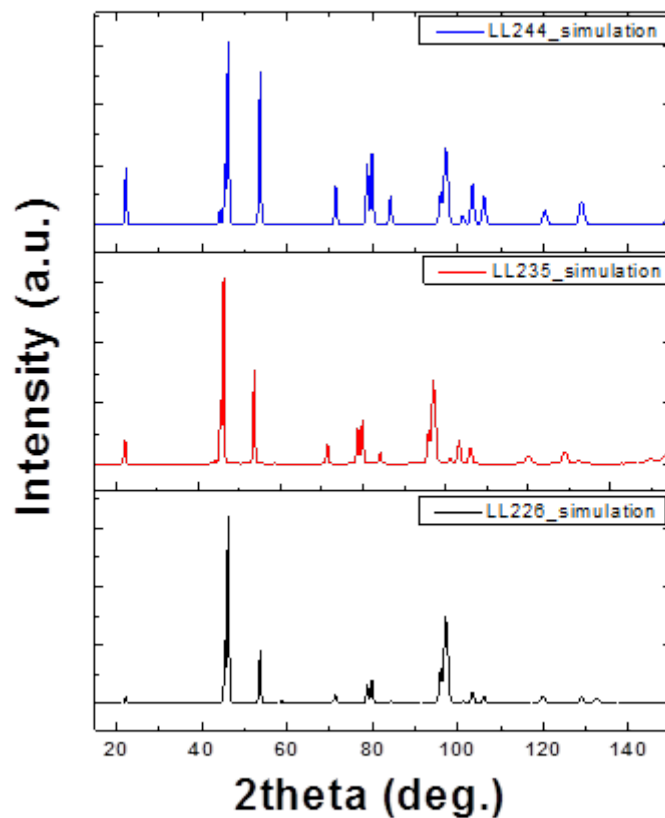
Figure S1. Simulated neutron diffraction patterns of LL226, LL235, and LL244.
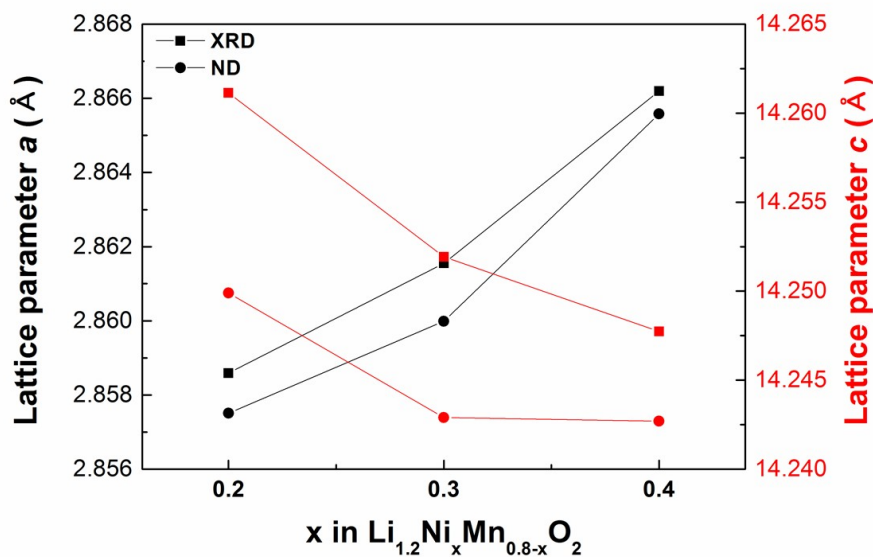
Figure S2. Lattice parameters of LL226, LL235, and LL244 observed by XRD and ND analyses. When only ionic size is considered, lattice parameters a and c should be larger in LL226. However, lattice parameter

a is larger in LL244, while lattice parameter c is larger in LL226 as expected. Anisotropic changes of a and c lattice parameters are attributed to the Jahn-Teller distortion of Ni^{3+} ion. The Jahn-Teller effect distorts the octahedral Ni of $LiNiO_2$ and splits Ni-O bonds into four 1.91Å bonds and two 2.09 Å bonds,[1] which makes the lattice expand in a and b axes and contract in c axis.
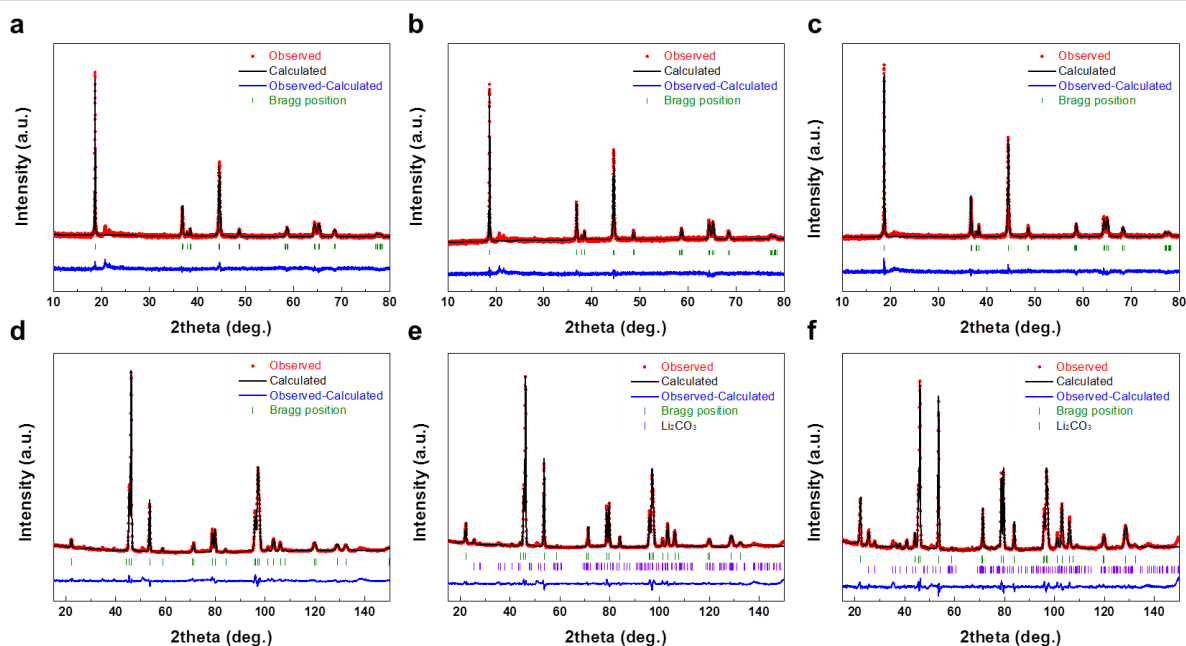
Figure S3. Rietveld refinements of the a, b, c) XRD patterns and d, e, f) ND patterns of LL226, LL235, and LL244 (left to right). R-factors for XRD and ND patterns are represented in Table S1 and S2.
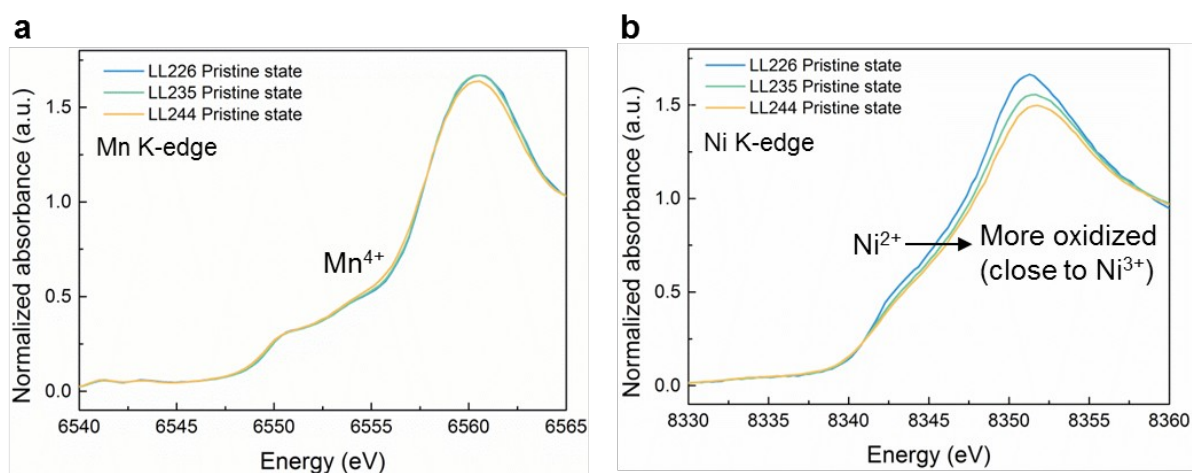
Figure S4. a) XANES Mn K-edge spectra, and b) XANES Ni K-edge spectra of pristine LL226 (blue), LL235 (green), and LL244 (orange). Mn and Ni K-edge spectra were collected in transmission mode with employing a Si(1 1 1) double crystal to monochromatize the X-ray photon energy. The monochromator was detuned to 35–45% of its original intensity to eliminate the high-order harmonics. Energy calibration was performed using the first inflection point of the spectra of Mn and Ni metal foils as a reference (i.e., Mn K-edge = 6539 eV and Ni K-edge = 8333 eV). Reference spectra were simultaneously collected for each *in situ* spectrum using Mn or Ni metal foils.
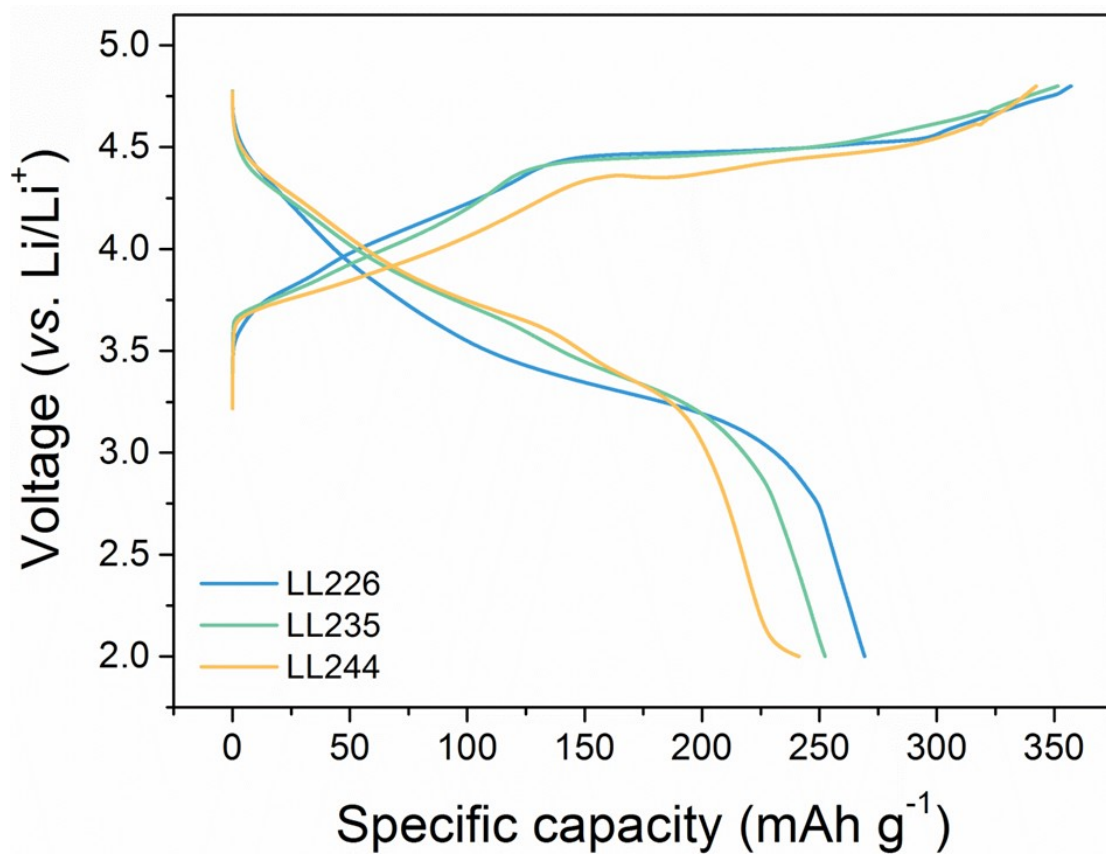
Figure S5. First charge/ discharge profile of LLNMO. Blue, green, orange denote LL226, LL235 and LL244 respectively.
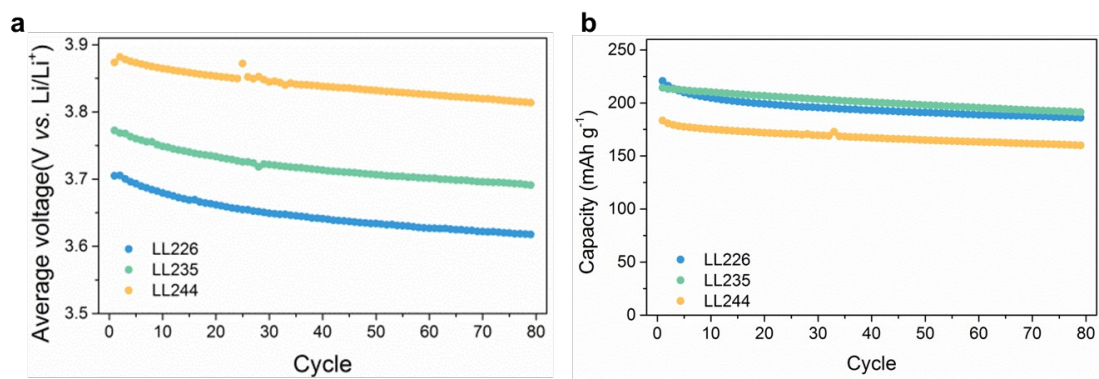
**Figure S6.** a) Average voltage and b) capacity retention of LLNMOs during 80 cycles at 1C rate.
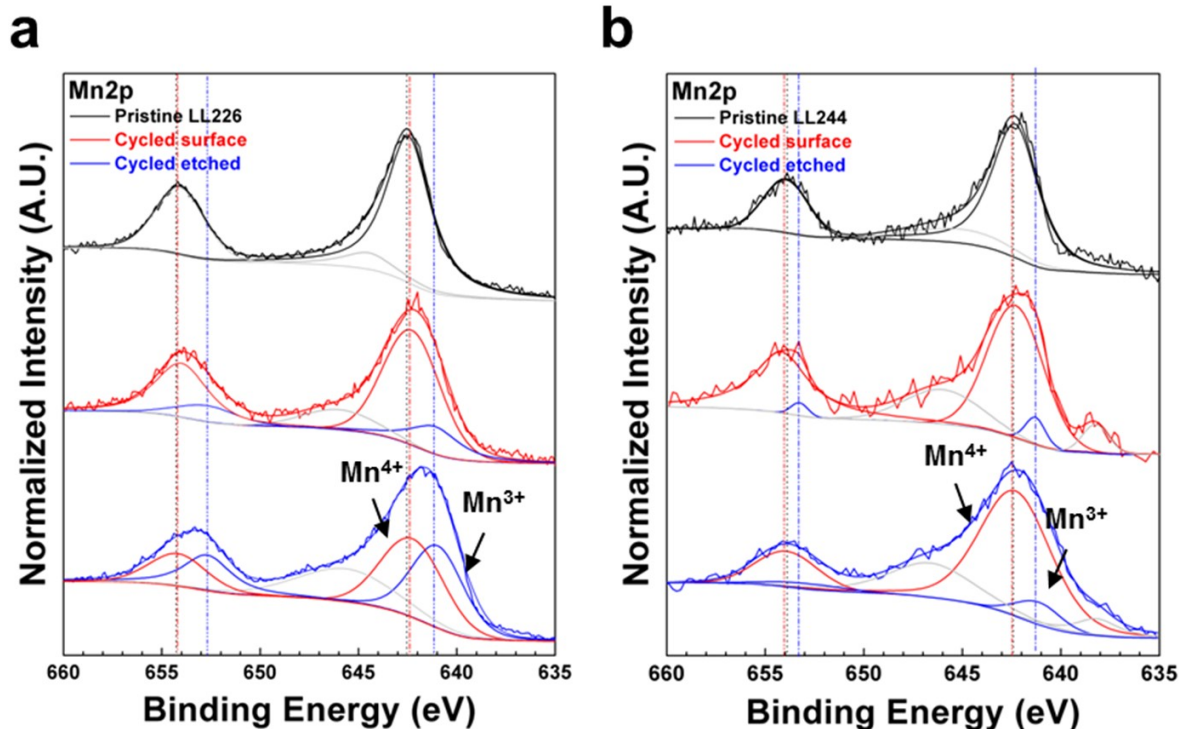
Figure S7. XPS Mn 2p spectra of a) LL226 and b) LL244. The black, red, and blue spectra (from top to bottom) represent the observed spectra of pristine LLNMO, the surface of cycled LLNMO, and an etched plane (surface + bulk properties) of LLNMO electrodes, respectively. The Mn 2p spectra of the etched planes show the reduction of Mn ions to the trivalent state after cycling. The activation of Mn dominantly occurred in LL226 rather than in LL244.
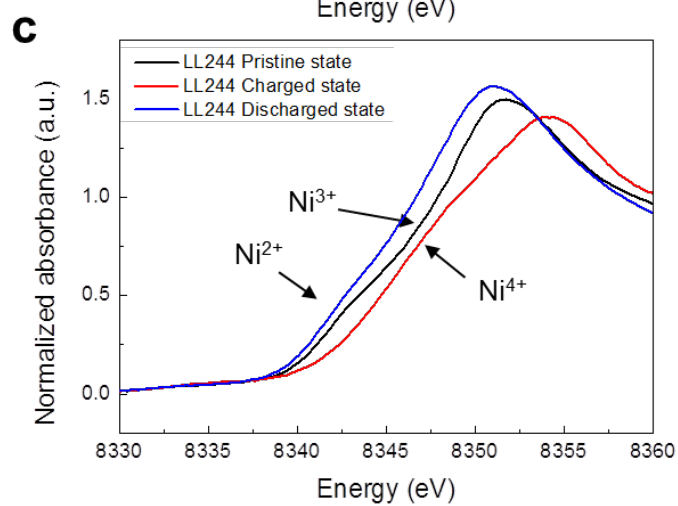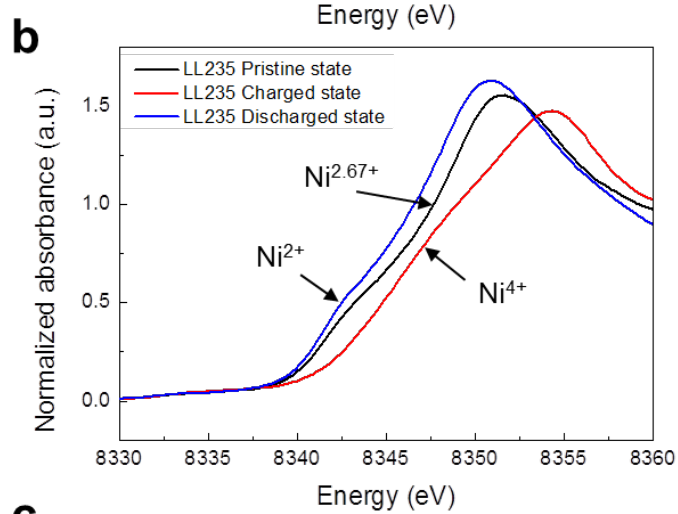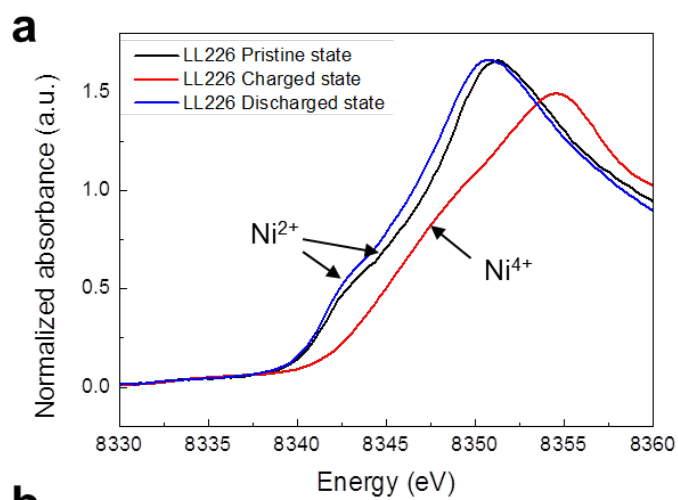
Figure S8. Ni K-edge XANES spectra of a) LL226, b) LL235, and c) LL244 electrodes at pristine (black), charged to 4.8 V (red), and discharged to 2.0 V (blue). Nickel divalent/tetravalent redox reactions occur in all compounds regardless of initial oxidation states of nickel ions.

$R\overline{3}m$ (110) plane   C2/m (020) plane   Fd-3m (220) plane
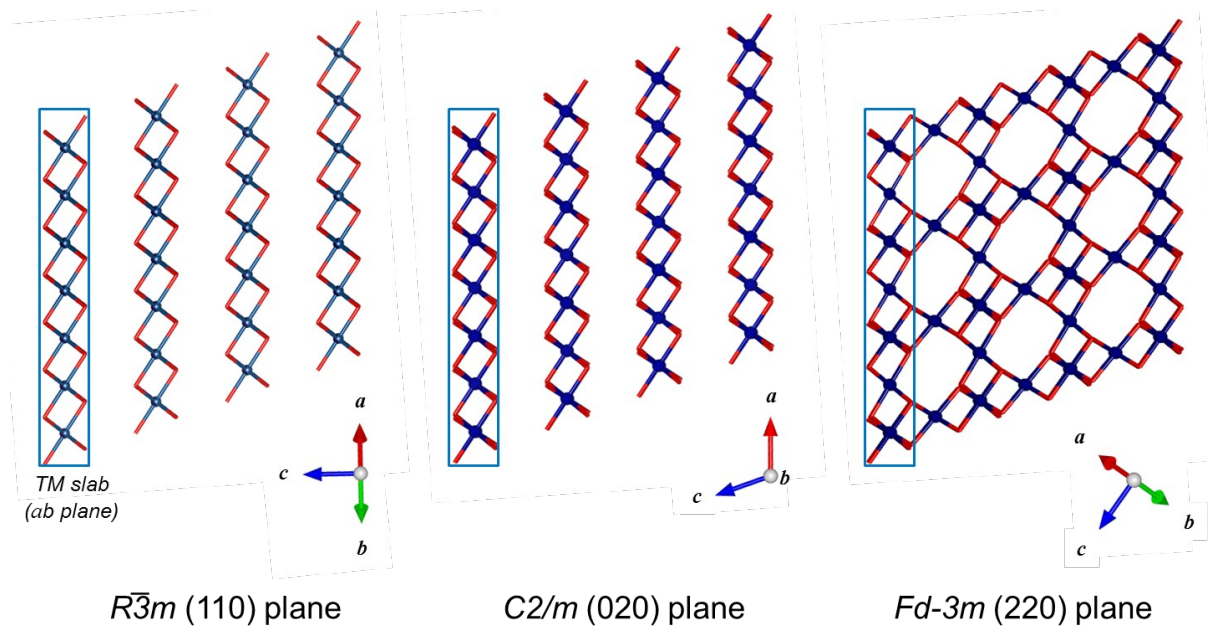
Figure S9. Structural differences between the layered $(110)_R//(020)_M$ planes and spinel $(220)_C$ plane. The formation of spinel-like phases in LLNMO after cycling takes place by the interlayer migration of the transition metal ions between the transition metal slabs.
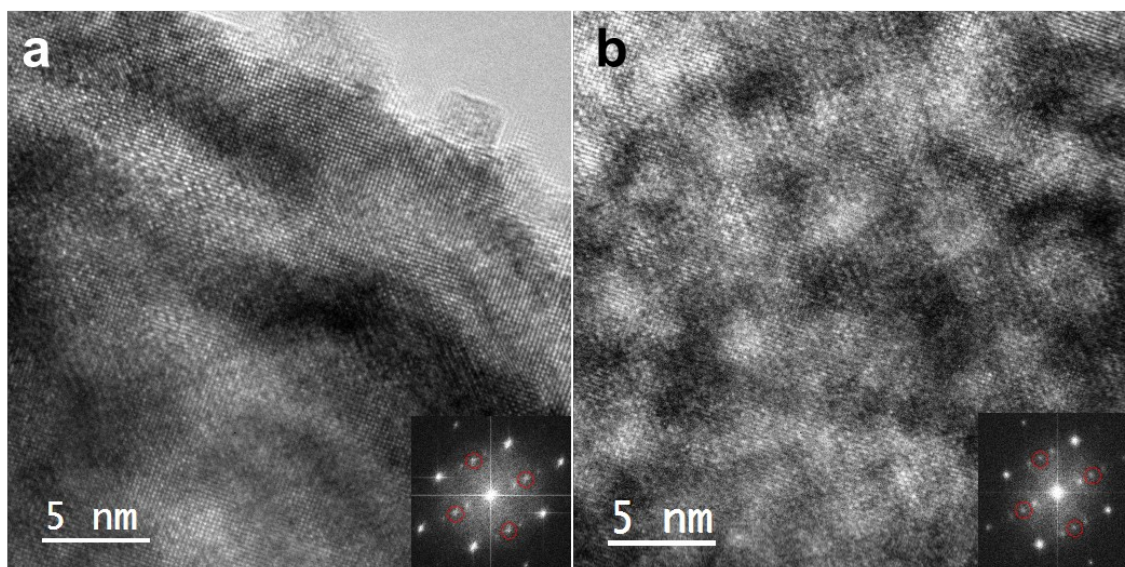
Figure S10. HR-TEM images and corresponding Fast Fourier transform (FFT) images of cycled LL226. Red circles in the FFT images denotes the {220} planes of the cubic spinel phase.
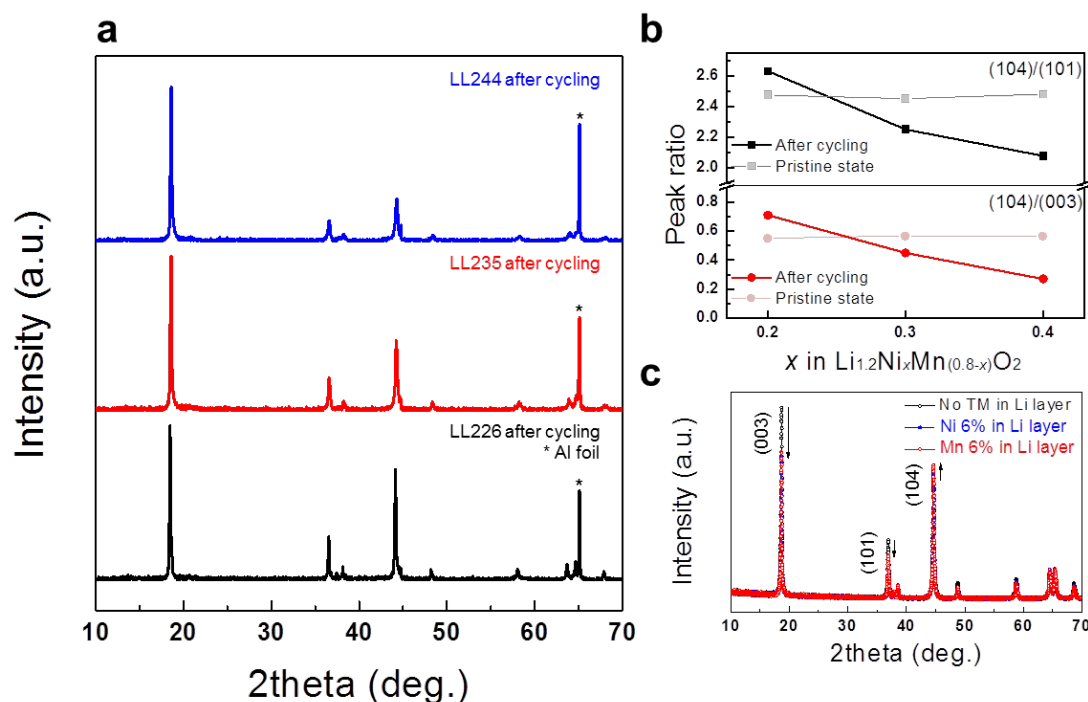
Figure S11. a) XRD patterns of LL226 (black), LL235 (red), and LL244 (blue) after five electrochemical cycles. b) Peak ratio of (104)/(101) (black) and (104)/(003) (red) of LLNMOs before and after cycling. c) Simulated XRD patterns of LLNMO with no transition-metal ions in Li layers (black) and with 6% Ni (blue) or Mn (red) migration into Li layers.

  The overall structural evolution was examined using XRD, and the results are presented in Figure S10. The most obvious difference in the XRD patterns of the LLNMOs after cycling is the ratio among several important Bragg peaks, which indicates the degree of transition-metal ordering.[2, 3] In the XRD patterns of LL226 after cycling, the intensity ratio of the (003)/(104) peak became notably smaller compared with those of LL235 and LL244, as observed in Figure S10a. For a clear comparison, we plotted the ratio of the (104) peaks at 44.1° to the (101) peaks at 36.5° and to the (003) peaks at 18.5° for LLNMOs in pristine states and after electrochemical cycling (Figure S10b). In the pristine states, the ratios of the (104) peak to the (101) and (003) peaks were almost identical for the three compounds in the ranges of 2.455–2.480 and 0.545–0.565, respectively. However, after five cycles, the peak intensities dramatically changed, which resulted in differences between the ratios for the LLNMOs with varying compositions. For LL226 with low Ni content, the ratios of the (104) peak to both the (101) and (003) peaks increased to 2.63 and 0.71,

respectively, whereas the values significantly decreased to 2.08 and 0.27, respectively, for LL244 with high Ni content. The increase of the ratios of LL226 is consistent with our simulated XRD patterns (Figure S10c), which qualitatively showed that the (104) peak grows whereas the (003) and (101) peaks diminish as some portion (~6%) of the transition-metal ions migrate into the Li layer, reducing the contrast between the transition-metal and lithium layers. In contrast, the decrease of the ratios of LL244 indicates the increased contrast between the transition-metal and lithium layers, which might originate from the lattice densification of the transition-metal layers. Previous NMR and XRD studies have revealed the substitution of vacancies (the original Li sites in transition-metal layers) with migrated transition-metal species. [4, 5]
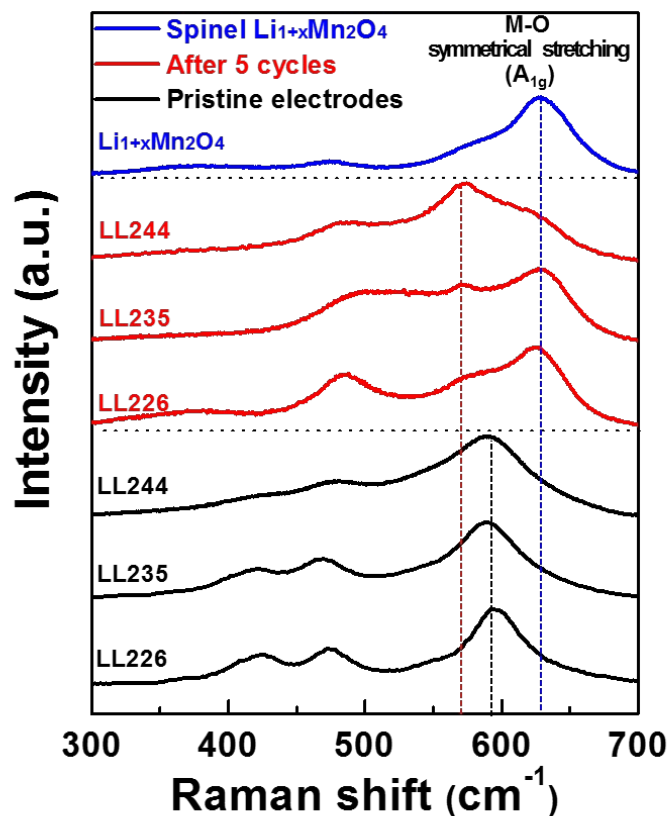
Figure S12. Raman spectra of LLNMOs before (black) and after five cycles (red) compared with spinel $Li_{1+x}Mn_2O_4$ (blue). Red dotted line and blue dotted line indicate A_{1g} mode of layered and spinel phases, respectively. The two peaks near 595 and 474 cm^{-1} correspond to the A_{1g} (symmetrical stretching of M–O) and E_g (symmetrical deformation) vibrational modes in layered lithium transition metal oxides with $R\bar{3}m$ symmetry, and the small peak at 425 cm^{-1} originates from the Li_2MnO_3-like structure with the lower $C2/m$ symmetry. The intensity of the peak at 425 cm^{-1} increased with increasing Mn content in the samples, implying a higher degree of ordering, which is consistent with the observation of the superstructure patterns in the XRD results (Figure 2a). The single A_{1g} mode for the pristine compounds indicates that the layered $LiMO_2$ and Li_2MnO_3 phases share a common layered lattice framework. The peak shift of A_{1g} mode of the pristine layered structure after cycling reflects the increase in the average mass of the atoms in the transition metal layers, which might be induced by the lattice densification. The densification is

also consistent with the disappearance of the peak at 425 cm^{-1}, corresponding to the honeycomb-like ordering in the transition metal layers in our Raman study as well as the XRD results (Figure S10).

References

[1]   A. Rougier, C. Delmas, A. V. Chadwick, *Solid State Commun.* **1995**, *94*, 123.

[2]   T. Ohzuku, A. Ueda, M. Nagayama, Y. Iwakoshi, H. Komori, *Electrochim. Acta* **1993**, *38*, 1159.

[3]   O. Tsutomu, M. Yoshinari, *Chem. Lett.* **2001**, *30*, 744.

[4]   N. Tran, L. Croguennec, M. Ménétrier, F. Weill, P. Biensan, C. Jordy, C. Delmas, *Chem. Mater.* **2008**, *20*, 4815.

[5]   M. Jiang, B. Key, Y. S. Meng, C. P. Grey, *Chem. Mater.* **2009**, *21*, 2733.